50th AIAA Aerospace Sciences Meeting including the New Horizons Forum and Aerospace Exposition
09 - 12 January 2012, Nashville, Tennessee
AIAA 2012-0822

Fundamental Processes of DBD Plasma Actuators Operating at High Altitude

Timothy G. Nichols[1] and Joshua L. Rovey.[2]
Missouri University of Science and Technology, Rolla, MO 65409

Dielectric barrier discharge (DBD) plasma actuators are active flow control devices being investigated for implementation on future aircraft. This paper provides the details of a high altitude analysis done on a plasma actuator operating at altitudes from 0 to 18288 meters (60000 feet) in order to qualitatively determine the fundamental processes that lead to increased power consumption and decreased force production. The actuator is driven with a 5 kHz sine wave with a peak-peak voltage of 13.4 kV at pressures of 760, 429, 321, 226, and 88 Torr. A passive measurement technique called the capacitive V-dot probe is adapted to the actuator in order to resolve the spatiotemporal evolution of the surface potential on the dielectric surface. At low pressures, where there is up to 800% more plasma than at sea level, the electric field is at or very near zero for approximately 80% of the dielectric surface, compared to just 55% at sea level. This implies that at lower pressures increased actuator power is spent making plasma and not accelerating it. Measurements also show that the location of the peak physical charge deposition corresponds closely with the location of the peak surface potential, indicating that the primary mechanism for building potential on the dielectric surface is due to physical charge deposition and not from the capacitive voltage division/polarization effects of the actuator.

Nomenclature

C_1	=	capacitance between the exposed electrode and the dielectric surface [F]
C_2	=	capacitance between the dielectric and the buried electrode [F]
C_3	=	capacitance due to geometric arrangement of plasma actuator [F]
C_{int}	=	op-amp integrator capacitor value [F]
d	=	dielectric material thickness
e	=	electric charge [C]
ε_r	=	dielectric constant
ε_o	=	permittivity of free space $\left[\frac{C^2}{Nm^2}\right]$
$\vec{E}$	=	electric field $\left[\frac{V}{mm}\right]$
$\vec{F}$	=	induced force [N]
K_1	=	calibration factor due to charging of bulk capacitance $\left[\frac{V}{kV}\right]$
K_2	=	calibration factor due to charging of dielectric surface $\left[\frac{V}{kV}\right]$
K_3	=	calibration factor due to polarization charging of dielectric surface
n_i	=	ion density $\left[\frac{number\ of\ ions}{mm^3}\right]$
P	=	power $[W]$
p	=	pressure [Pa]
V	=	plasma volume $[\frac{1}{m^3}]$
R_{int}	=	op-amp integrator resistor value [Ω]

[1]Graduate Research Assistant, Department of Mechanical and Aerospace Engineering, 160 Toomey Hall, 400 West 13th Street, Student Member AIAA
[2] Assistant Professor of Aerospace Engineering, Department of Mechanical and Aerospace Engineering, 292D Toomey Hall, 400 West 13th Street, Senior Member AIAA

σ = surface charge density $\left[\frac{C}{m^2}\right]$
V_{probe} = V-dot probe signal [V]
V_{surf} = surface potential due to charge deposition [kV]
V_{net} = total surface potential on dielectric surface [kV]
V_{Max} = potential due to capacitive voltage division and polarization effects of dielectric material [kV]

I. Introduction

Single dielectric barrier discharge (SDBD) plasma actuators have shown promise as reliable and easy to use active flow control devices [2-4] **.** The induced flow that the actuator produces has been shown to delay stall and separation over an airfoil, in turn maintaining lift at high angles of attack [2, 5-8]. SDBD plasma actuator parameters such as material thickness, type of dielectric material used, applied waveform shape and frequency, and actuator geometry configuration have been shown to affect the discharge characteristics and therefore the effectiveness of the actuator [9-13].

The SDBD plasma actuator consists of a dielectric material and two electrodes arranged in an asymmetrical geometry. A schematic of a typical plasma actuator configuration is shown in Figure 1. Copper tape is most commonly used for the electrodes, while glass, Kapton tape, Teflon, and Macor ceramic are commonly used as the dielectric material. One electrode is placed on the dielectric surface exposed to ambient air conditions, while the other electrode is grounded and covered (or buried) by a dielectric material on the opposite side of the dielectric. These electrodes are referred to as the exposed and buried electrodes, respectively. To operate an actuator, a high frequency high voltage AC waveform (from a few kilovolts to tens of kilovolts; frequencies in the kHz range) is applied between the electrodes. During the operation of the plasma actuator, the plasma ignites and extinguishes itself twice. The first half cycle, called the forward stroke, is when the voltage on the exposed electrode is negative going. During this half of the cycle electrons are transferred from the electrode to the dielectric surface. These electrons collide with neutral air particles creating ions and forming the plasma. The plasma then quenches and the voltage goes from being negative to positive. During the back stroke, or positive-going voltage, electrons are drawn back to the exposed electrode from the dielectric surface. They again collide with neutral air particles causing the second ignition of the plasma. The plasma quenches again when the voltage is no longer positive-going. As plasma ions are created they are simultaneously accelerated by the electric field between the electrodes. Ions transfer momentum to the surrounding neutral air molecules through collisions, creating an induced flow tangential to the dielectric surface. This flow is the mechanism for aerodynamic control by the actuator. Momentum transfer collisions occur close to the dielectric surface, usually in the sub-boundary layer region. Gregory *et. al.* have shown that the body force produced by a plasma actuator is due to the acceleration of plasma ions through an applied electric field and the subsequent collisions with neutral particles [14]. This force is governed by ion density, volume of the plasma, and the applied electric field, as is shown in Eq. (1).

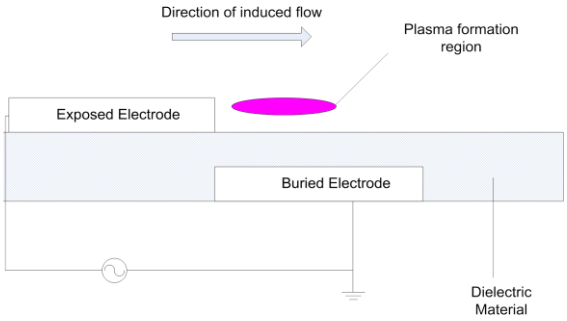

Figure 1. Schematic diagram of a DBD plasma actuator. The induced flow is the mechanism by which the actuator controls air flow.

$$< \vec{F} >= \int \int en_i(\vec{r},t)\vec{E}(\vec{r},t)d\vec{r}dt \quad (1)$$

The amount of force produced by a SDBD plasma actuator depends heavily on a number of parameters already mentioned previously in this paper. The environment in which the actuator is operated is one of the most influential of these parameters that can affect the overall performance of the actuator. Operating a plasma actuator in a low pressure environment leads to an increase in power consumption, a larger plasma formation region, and an induced flow velocity that initially, but then decreases [14-21]. Gregory *et. al.* found a linear relationship between force production and the ambient atmospheric conditions, with the force going to zero in vacuum conditions [14]. They also found a nonlinear relationship between electric field strength and pressure, attributing the decrease in field

strength as pressure decreases to the variation of breakdown voltage as the neutral density changes. Similar results regarding the change in the average electric field were found by Litvinov *et. al.* [15]. They also demonstrated that there is an increase in force production down to pressures of 200 Torr due to an increase in the volume of the plasma. This leads to an increase in the number of plasma ions available for momentum transfer. Following this study, Benard *et. al.* used Pitot tube measurements to show that the induced velocity increases as the pressure drops from 760 Torr, where the velocity is 2.5 m/s, down to 456 Torr, where the velocity is 3.5 m/s [16, 17]. Pressures below 456 Torr show the induced velocity decreasing. Another study performed by Benard *et. a.l* found an increase in electric wind velocity down to pressures of 350 Torr at which point the induced velocity began decreasing [16]. An increased mass flow rate can be achieved down to pressures of 350 Torr by increasing the grounded electrode length, but at lower pressures this affect becomes greatly reduced. A study performed by Wu *et. al.* produced results that show a maximum induced velocity of approximately 1.5 m/s at 445 Torr, which is in good agreement with Benard *et. a.l* [17, 18]. They also showed that below 45 Torr the plasma formed on the dielectric surface switches from a filamentary dominated discharge to a glow dominated discharge. This is an important result because in the filamentary mode the electron density decreases with pressure while the electron temperature remains unchanged. The glow mode, however, produces an increase in both electron temperature and electron density as pressure decreases. Abe *et. al.* demonstrated the highly non-linear fashion in which ambient pressure affects the induced velocity [19]. Their study also showed a slight increase in actuator performance in a carbon dioxide gas environment versus a nitrogen gas environment. Another study performed by Benard and Moreau also showed that a decrease in pressure results in increased power consumption as well as an increase in induced flow velocity from 3 m/s at 760 Torr to 5 m/s at 287 Torr (26247 feet in altitude).

To gain a better understanding of the fundamental operation of the plasma actuator it is necessary to study the correlation between operating parameters and the plasma actuator actuation characteristics. In this study the actuator is operated in a simulated high altitude environment in order to understand the affects of low pressure on the overall charge deposition, dielectric surface potential, electric field strength, and force production. In Section II the experimental techniques used to measure the surface potential and electric field strength, as well as the overall experiment setup, is described. Section III provides the results obtained from the experiment. Section IV provides a discussion of the results followed by conclusions in Section V.

II. Experimental Techniques and Setup

Understanding the experimental procedure requires an understanding of how charge buildup on the dielectric surface leads to plasma formation. The discharge mode of the DBD exists as discrete micro discharges, not as one continuous discharge [4]. Microdischarges deposit charge onto the dielectric surface which reduces the applied electric field at that particular location. This limits the region of expansion of the plasma and is the cause for its self-limiting behavior. Furthermore, the structure of the plasma has been shown to be vastly different between the forward and backward strokes [22]. The electric potential at the exposed electrode is well-defined since it is equal to the applied potential. Likewise, the potential on the buried electrode is known (in this configuration it is the ground reference). The potential build-up on the surface of the dielectric, however, depends on two things: the capacitance division that is inherent in the actuator design and the surface-plasma interaction[23, 24]. Even when there is no breakdown and plasma does not form, the presence of some non-zero potential is present due to the polarization effect of the dielectric.

To determine the potential on the dielectric surface as a function of time and space, the buried electrode is broken into 14 electrically isolated segments (shown in Figure 2) which are grounded through an op-amp based active integrator circuit, as opposed to being grounded directly. An electrically isolated segment and the corresponding active integrator circuit together make-up what is called a V-dot probe. A schematic of this setup is shown in Figure 3. Each V-dot probe is 2.5 mm x 5 cm with the entire array of 14 probes arranged in a staggered formation. Since the plasma extent grows as the ambient pressure decreases, the probe array is spaced such that the surface potential and electric field far from the exposed electrode edge can be calculated. The numbered probes in Figure 2 correspond respectively to downstream distances of x = 1.00, 2.25, 3.5, 4.75, 7.5, 9.75, 12.5, 14.75, 20, 24.75, 30, 34.75, 40, and 44.75 mm. For the data acquired and shown in this paper, only one V-dot probe and integrator circuit is used at a time. One V-dot probe is passed through the vacuum chamber via a BNC-BNC pass through while the other 13 probes are shorted directly to ground, not through an integrator circuit. In this way the surface potential is stitched together from running the actuator at the same operating condition 14 different times. To ensure that the plasma discharge propagates downstream as it would with an un-segmented buried electrode, the copper surrounding the V-dot probes is also grounded.

The integrator circuit sums the current that is due to the charging of the bulk capacitance as well as the current that charges the dielectric surface. The former of these effects does not contribute to the surface potential buildup on the dielectric which is why it is necessary to calibrate the circuit response for each of these effects separately. This is done through two different calibrations, described below.

A. Capacitive V-Dot Probes

A thorough explanation of the setup and use of the capacitive V-dot probe is given in [24, 25]. A brief overview of the method and its implementation is given here. To make a V-dot probe, a section of the encapsulated electrode is segmented and electrically isolated from the rest of the electrode. This particular segment is then connected to an op-amp-based active integrator circuit, which is shown in Figure 3. As was previously mentioned, the plasma actuator consists of three different capacitances, shown in Figure 4, that give rise to three different displacement currents. The integrator circuit produces an output signal that is proportional to all of these displacement currents. Through two different calibrations it is possible to back out the displacement current that is due only to physical charging of the dielectric surface. These two calibrations alone, however, do not give the entire surface potential present at the dielectric surface. The capacitive voltage division that is present due to the actuator geometry, as well as the polarization effects of the dielectric material, contribute to the net surface potential on the dielectric. These effects are readily calculated by solving Laplace's equation with the appropriate boundary conditions. By adding these effects to the surface potential due to charge deposition by the plasma, it is then possible to determine the surface potential at any of the V-dot probe locations.

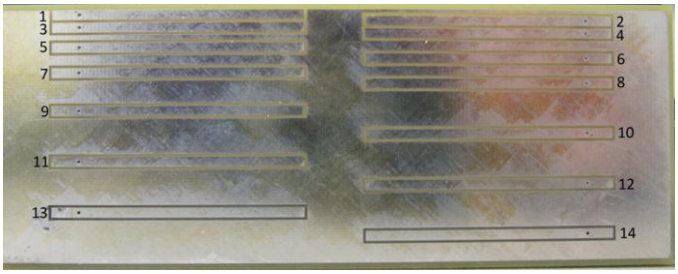

Figure 2. The segmented buried electrode. The spacing of the electrodes is such that at low pressures the charge on the dielectric surface can be measured over the entire extent of the plasma, not just close to the exposed electrode.

An analysis of any one of the signals from a particular op-amp integrator circuit is performed in the following steps. Using the first calibration factor, K_1, the displacement current due to bulk charging is subtracted from the raw signal received from circuit. The remaining current is due to the physical charge deposition onto the dielectric surface. Using the second calibration factor, K_2, it is possible to determine the surface potential due to this charge buildup. Letting $V_{probe,i}(t)$ be the signal from the i^{th} probe, the surface potential at a probe location, $V_{surf,i}(t)$, due to charge accumulation on the dielectric surface with an applied waveform $V_{ac}(t)$ is given by Eq. 2. The total surface potential, $V_{net,i}(t)$, is then found by adding $V_{surf,i}(t)$ to the surface potential due to the capacitive voltage division/polarization effect of the dielectric material, V_{Max}, as is shown in Eq. 3. The amount of charge that is physically deposited onto the surface of the dielectric is readily calculated using Eq. 4.

It is important to note that the op-amp integrator signal is an integral over time with respect to an initial starting condition. Therefore, it is necessary to start each measurement from a known starting condition, that is, an uncharged dielectric surface. To achieve this, a solvent (in this experiment, acetone) is used to wipe the surface of the actuator to remove the long living DC charge [26] that exists between runs of the actuator.

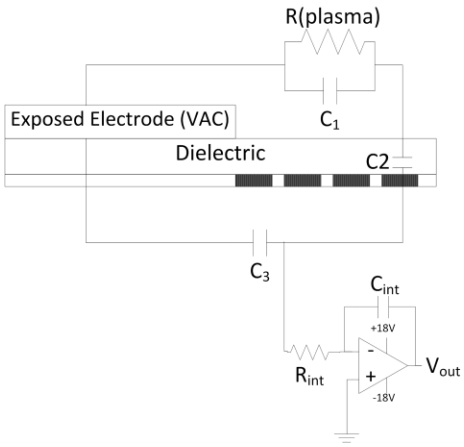

Figure 3. Each buried segmented electrode is connected to an op amp integrator circuit with a large resistor in parallel (50 MΩ in this experiment) with the integrating capacitor, C_{int}.

$$V_{surf,i}(t) = \frac{V_{probe,i}(t) - K_1 V_{ac}(t)}{K_2} \tag{2}$$

$$V_{net,i}(t) = V_{surf,i}(t) + V_{Max} \tag{3}$$

$$\sigma_i = (\frac{\varepsilon_r \varepsilon_o}{d}) V_{surf,i} \tag{4}$$

1.) Charging of the Bulk Capacitance – 1st Calibration

Production of the SDBD body force that allows for flow control comes from the creation and acceleration of ions. The acceleration of the ions occurs due to an electric field that originates at the exposed electrode and terminates on the buried electrode. Due to the geometry of the plasma actuator, it is necessary to include the capacitance C_3. This is because some electric field lines pass through the dielectric material and terminate on the buried electrode, directly connecting the two electrodes and providing a parallel path for additional displacement current to flow. It should be noted that although this current is always present in the circuit, it does not affect the overall plasma discharge. This capacitance does not contribute to the surface charging of the dielectric surface. Since the integrator circuit produces a signal that is due to the displacement current through all three of the capacitances shown in Figure 4, the portion of the signal from the integrator circuit that is due to the charging of C_3 must be subtracted off. This value (referred to as the "bulk capacitance") requires running the actuator at a low voltage (less than the required voltage needed to generate plasma.) Doing this for each V-dot probe comprises the 1st calibration and gives the calibration factor, K_1, for each probe. The response of a given probe to an applied waveform is linear to within ± 0.3%, shown in Figure 5a. For a pressure of 760 Torr we find that K_1 varies from K_1 = 0.348 V/kV for the probe nearest the exposed electrode to K_1 = 0.007 V/kV at the probe farthest from the exposed electrode, as shown in Figure 5b. Since the actuator geometry and operating parameters remain constant, we would expect to see the same value for K_1 regardless of the ambient pressure. This is indeed what we find with the largest deviation being ± 0.18% for the probe nearest the exposed electrode (x = 1.00 mm).

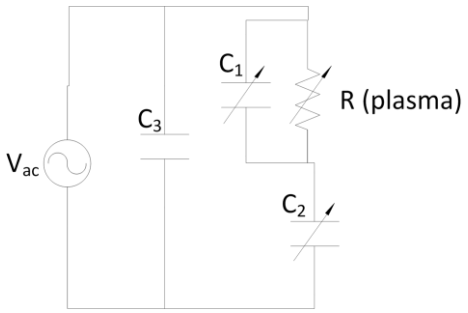

Figure 4. Lumped circuit model of the DBD plasma actuator (from Enloe *et. al.* [1]).

2.) Surface Charging – 2nd Calibration

Whereas the first calibration takes into account the displacement current that goes into charging the bulk capacitance, the second calibration is used to determine the amount of charge physically deposited on the dielectric surface by the plasma. In Figure 4, C_1 is the capacitance between the exposed electrode and the dielectric surface. The capacitance C_2 is located between the dielectric surface, which serves as a virtual electrode, and the buried physical electrode. Since the plasma extent in the downstream direction changes during operation, the capacitances C_1 and C_2 will as well; this is why they are represented as variable elements in Figure 4. At breakdown (i.e. when plasma is present), a resistive path (R) becomes present from the exposed electrode to the dielectric surface. This current cannot penetrate the dielectric material (unlike the current in the first calibration). In keeping with the current literature [24] this volume is broken into two different capacitances, labeled C_1 and C_2 in Figure 4. With plasma present current flows through R charging C_1 which creates another displacement current that the integrator circuit will measure. It is possible to determine the V-dot probe response to this displacement current by running the actuator at low voltages with a temporary extension of the exposed electrode over the dielectric surface. The extended electrode serves to mimic the effect of surface potential due to charge buildup on the surface. This extension of the exposed electrode is realized by covering the surface of the dielectric with copper tape. This calibration factor relates the V-dot probe output voltage to the charge accumulation on the dielectric surface. Since each probe in this experiment has identical dimensions the second calibration factor should be the same for each V-dot probe. This is what we find with K_2 at atmospheric conditions being K_2 = 0.257 V/kV where the percent difference between all probes is ± 9.7%.

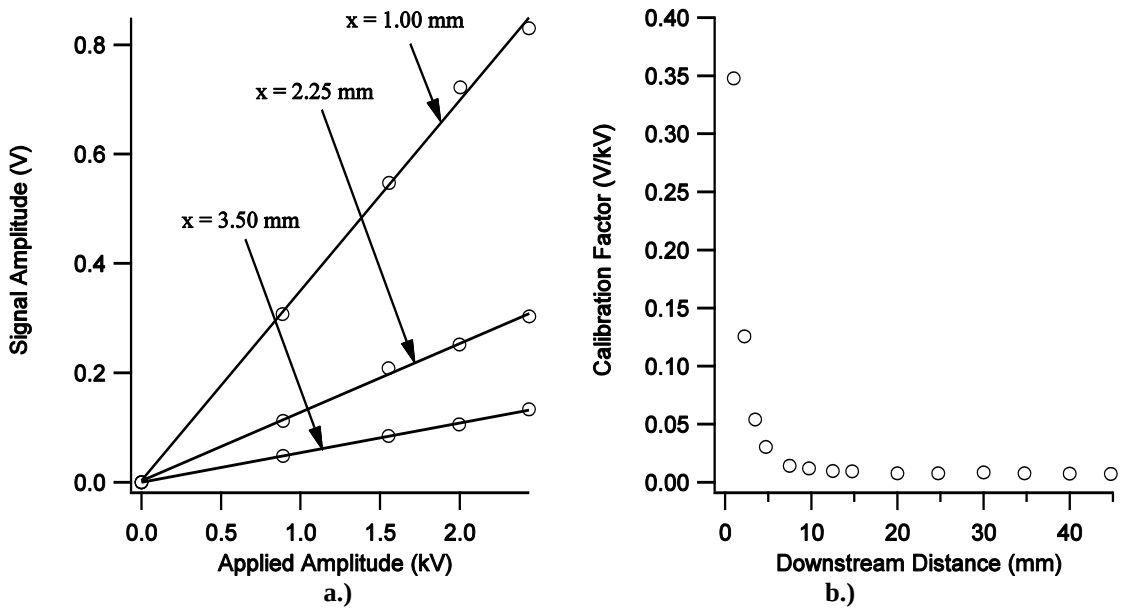

Figure 5. Response of the V-dot probes to the charging of the bulk capacitance, K_1.

3.) Charge Due to Capacitive Voltage Division and Polarization of Dielectric Material

Using the first and second calibrations and Equation 2 it is possible to determine the amount of charge being deposited on the dielectric surface. The total potential on the dielectric surface, however, is due not only to the deposited surface charge, but also to the polarization created by the dielectric surface. Additionally, the applied potential on the exposed electrode is capacitively divided by C_1 and C_2 even when plasma is not present. Accounting for this is straight forward and is calculated by solving Laplace's equation with the appropriate boundary conditions. The program Ansoft Maxwell is used to perform these calculations and provides the unit-less third calibration factor, K_3. The value of K_3 ranges from $K_3 = 1$ right at the exposed electrode edge to $K_3 = 0.00205$ at the last V-dot probe. By adding the contributions to the potential from the polarization effect and deposited charge on the dielectric surface, the total potential on the dielectric surface at 14 different spatial locations can be determined (Equation 3). Using these data it is then possible to determine the electric field downstream from the exposed electrode.

B. Plasma Actuator

The plasma actuator used in this study has a standard asymmetrical geometry between the exposed and encapsulated electrode with a 1.6 x 305 x 305 mm piece of Macor ($\varepsilon_r = 6$) between them. The length of the exposed electrode is 138 mm with a width (measured in the streamwise direction) of 17.3 mm. The buried electrode has a total downstream length of 52 mm with 14 electrically isolated V-dot probes that have dimensions of 2.5 mm x 5 cm. By using the spacing shown in Figure 2 it is possible to measure the potential on the dielectric surface up to 44.75 mm downstream from the exposed electrode. Additionally, by using a Tektronix P6015 high voltage probe it is possible to measure the potential on the exposed electrode itself, thereby providing a fifteenth data point in the potential distribution across the dielectric surface. A picture of the actuator used in this experiment is shown in Figure 6.

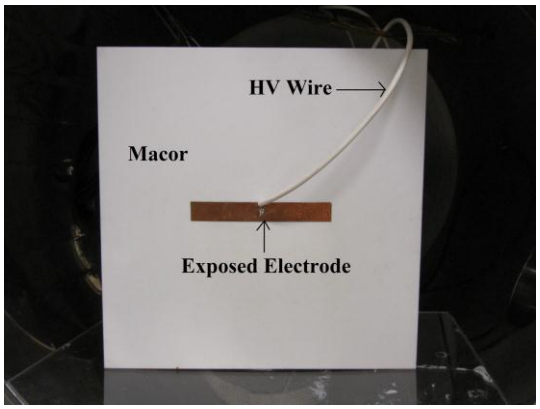

Figure 6. The large Macor dielectric provides enough surface area as to prevent arcing at low pressures.

A simple block diagram showing the components of the actuator electrical system is shown in Figure 7. Operation of the plasma actuator uses a Rigol DG 1022 function generator which is connected to a Crown CE 2000 amplifier. The signal from the amplifier is stepped up to kilovolt level with

a CMI-5525 high frequency transformer. This transformer has a turn ratio of 1/357, a frequency range of 900 Hz – 5 kHz, and is capable of outputting up to 25 kV at 0.2 A_{rms}. A Pearson 4100 current monitor, placed around the common ground wire, is used to measure the total actuator current. It has a 10 ns rise time which, for this application, is accurate enough to measure the displacement current as well as to capture the microdischarge current spikes produced by the actuator that are indicative of plasma formation.

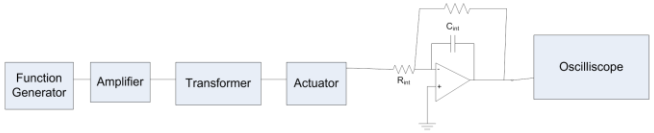

Figure 7. A 5 kHz sine wave is generated with the function generator and then stepped up through an amplifier and step-up transformer to kV levels. The integrator circuit output is fed to an oscilloscope.

C. V-dot Probe Electronics

The op-amp integrator circuit has a LF-411 op amp with $C_{int} = 11$ nF. A large resistor (in this experiment 50 MΩ) is placed in parallel with C_{int} such that the capacitor is completely bled off in between runs. This is important due to the necessity that the integrator start from some known (i.e. uncharged) state. The RC time constant for this circuit is 550 ms, which is much slower than the 0.2 ms applied waveform period. With this time constant and a known starting condition (i.e. an uncharged actuator surface) all aspects of the integrator circuit are valid, including the DC offset that occurs during the first period of the applied AC waveform.

Each V-dot probe is connected to ground (or the integrator circuit if being tested) with standard RG-58 coaxial cable and terminated with a 50 Ω BNC connector. The grounded shield of the cable is used to eliminate cross talk between the V-dot probes as well as to help lower the amount of ambient noise the signal picks up between the buried electrode and the integrator circuit. The probes that are shorted directly to ground are connected to a conducting box and grounded to the vacuum chamber (discussed below), which serves as the common ground for the entire experiment. Standard coaxial cable is again used to establish the ground connection between the grounding box and the common ground due to its low impedance characteristics.

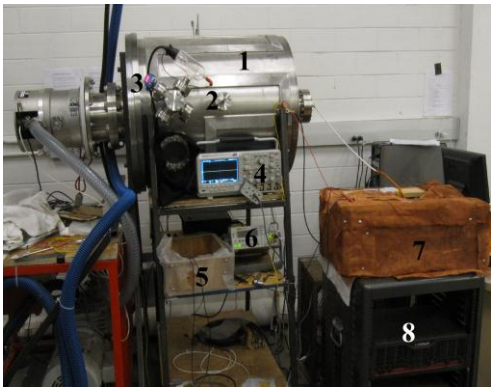

Figure 8. 1. Vacuum Chamber; 2. BNC-BNC Passthrough; 3. Lesker Pressure Gauge; 4. Tektronix DPO 2024 Oscilliscope; 5. Op-Amp Integrator Circuit; 6. Rigol Function Generator; 7. Faraday Cage; 8 High Voltage Probe

D. High Altitude Testing Setup

The entire experimental setup is shown in Figure 8. The high voltage wire from the step-up transformer connects to a high voltage pass through into the bell jar vacuum chamber. The ambient pressure is measured with a Lesker KJL275800 convection pressure gauge. The gauge has a pressure range of 1000 Torr down to 10^{-4} Torr. The signal from a V-dot probe is connected to a BNC pass through out to the integrator circuit. A Tektronix DPO 2024 oscilloscope is used to measure the output of the integrator circuit and to save the waveform data. The oscilloscope has a bandwidth of 200 MHz and is capable of acquiring 1 GS/s on a single channel. A Tektronix P6015 high voltage probe with a 1000:1 step down for the given experiment impedance is used to measure the voltage being applied to the exposed electrode. This also serves as a 15^{th} data point in our knowledge of the spatiotemporal potential deposition on the dielectric surface. A faraday cage houses the step-up transformer as well as the high voltage probe.

III. Results

The results of the V-dot probe measurements are shown here. Along with surface potential and longitudinal electric field results we also present a brief qualitative analysis of the effect that the ambient pressure has on the overall volume of the plasma. The time intervals used in this section correspond to those times labeled in Figure 9. Time t_1 corresponds to when the plasma is quenched and the change in applied potential is negative. As the applied waveform progresses the plasma ignites in the forward stroke at approximately time t_2 (50 μs after t_1). The plasma quenches again at time t_3 (100 μs after t_1), before it enters the backward stroke and ignites for the second time at time t_4 (150 μs after t_1). The applied waveform used to collect all data presented is a 5 kHz 13.4 kV_{pk-pk} sine wave.

A. Plasma Extension and Power Consumption

The qualitative plasma extent analysis and calculated power dissipation are presented in this section. In order to determine the effect that pressure has on the extent of the plasma formation region, qualitative photographs, such as those shown in Figure 11, were used. The exposure time for each picture was set at 1/3 s providing a time averaged photograph of the distribution of plasma on the surface of the dielectric. For each of the tested pressures (760, 429, 321, 226, 171, and 88 Torr), the plasma extends downstream from the exposed electrode a distance of approximately 7, 9.5, 14, 24, 38, and 56 mm, respectively. These results indicate a non-linear growth in the plasma extension as pressure is decreased, as seen in Figure 10, and shows good agreement with those presented by Benard *et al.* [16, 17]. It is also worth noting that as the pressure decreases more plasma is formed in the upstream direction of the exposed electrode. In other words, plasma is formed where there is no grounded electrode. Even at 760 Torr, plasma is formed on the corners of the exposed electrode in the upstream direction due to the strong electric fields that are present on the sharp points of the electrode edge. Note that the extent of the plasma has surpassed the length of the buried electrode at 88 Torr.

Power dissipation by the actuator at different pressures was calculated by operating the actuator with the same input parameters (13.4 $kV_{pk\text{-}pk}$, 5kHz frequency) and varying the pressure. Using Eq. 5, we are able to calculate the time averaged (over four periods of the applied waveform) power dissipation using the data from plots such as those shown in Figure 9. Using three different sets of data we determine that the average power draw varies, at most, by 20% for a given operating pressure. This is shown by the error bars in Figure 10. At 760 Torr the power consumed by the actuator is approximately 0.2 $\frac{W}{cm}$ whereas at the lowest tested pressure of 88 Torr, the actuator draws 1.1 $\frac{W}{cm}$. The non-linear increase in power as pressure decreases matches the trends seen by Benard *et al.* in their experiments [16, 17].

$$P = \frac{1}{N}\sum_{i=1}^{N} I_i V_i \tag{5}$$

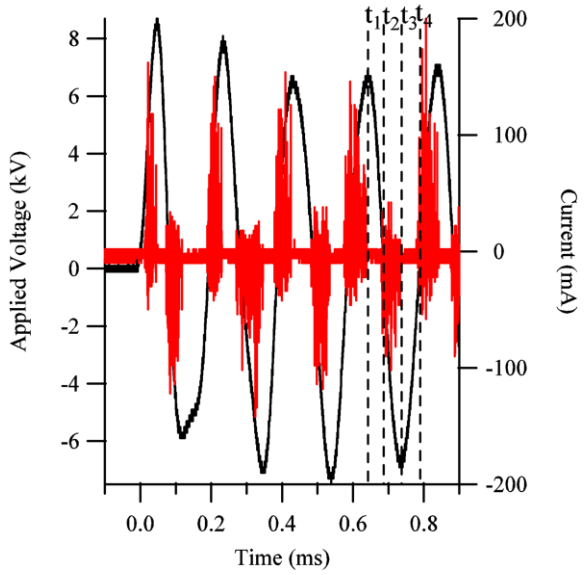

Figure 9. Applied waveform (black) and corresponding current plot (red) with four distinct time intervals labeled.

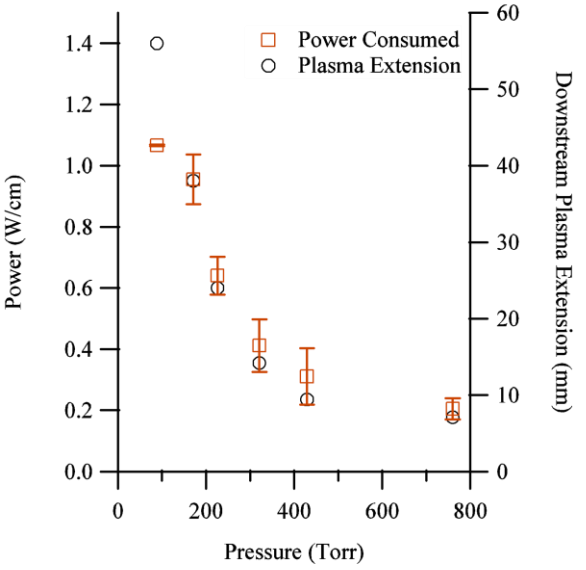

Figure 10. Decreasing the pressure increases power consumption and plasma to form farther downstream.

B. Surface Potential and Electric Field Measurements

Results in this section were obtained by applying Eq. (2) and (3) with the previously discussed calibrations to the raw V-dot probe measurements. All data were obtained for the first few cycles of the applied waveform with a clean actuator (surface wiped with acetone between shots). To reiterate, wiping the surface of the dielectric ensures that the displacement current being integrated by the integrator circuit is due solely to the plasma discharge and not to residual charge left from previous plasma shots.

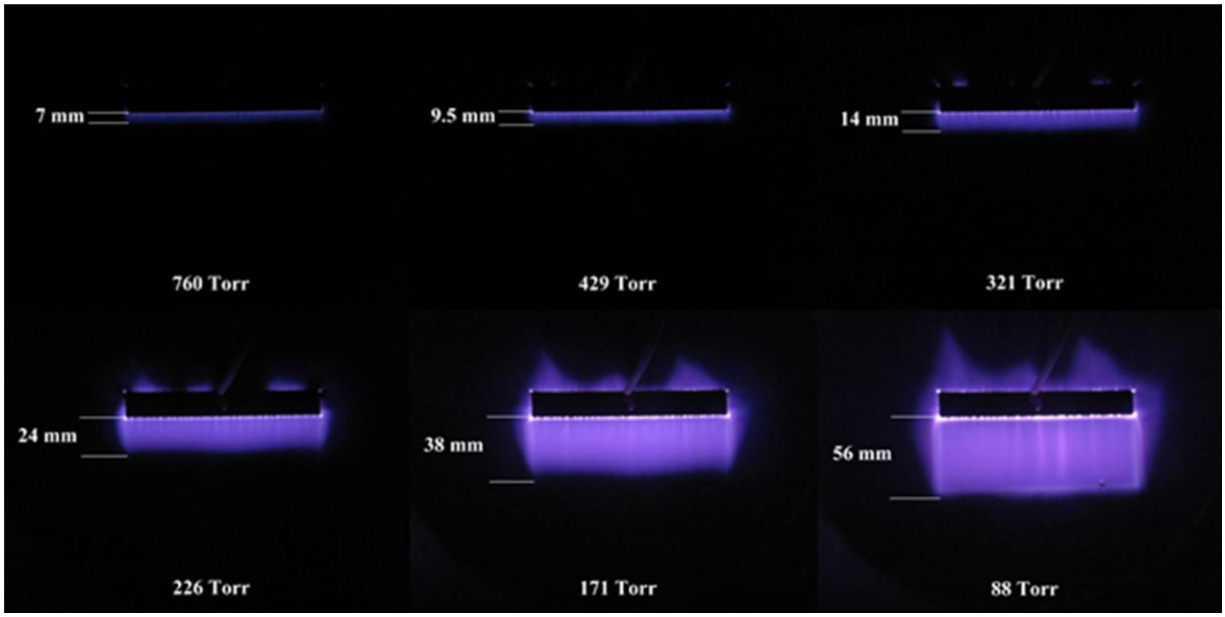

Figure 11. Pictures taken with 1/3s exposure time to give a time averaged view of the plasma distribution on the dielectric surface.

In Figure 12 the surface potential is plotted as a function of time and downstream distance. These plots provide an overview of the surface potential distribution and behavior. At 760 Torr the surface potential is highest closest to the exposed electrode. As pressure decreases the surface potential begins to spread out across the dielectric surface. This is indicative of more plasma being formed in the downstream location. Further evidence of this is the fact that in Figure 12 the peak surface potential decreases near the exposed electrode while downstream locations that had a surface potential of approximately zero (at 760 Torr) increase as pressure is lowered. This suggests that the electrons emitted from the exposed electrode (in the forward stroke; from the dielectric surface on the backward stroke) can travel greater distances before having collisions with neutral air or being deposited on the dielectric surface (as the mean free path increases with decreasing pressure).

While looking at the three-dimensional plots provides a good overview of the surface potential it is more beneficial to examine the surface potential distribution in discrete slices of time. These plots can be seen in Figure 13 - Figure 18, where the results for each pressure are shown as a single figure. The time intervals shown in these figures correspond to the times labeled in Figure 9. By looking at the surface potential at the four described time intervals it is possible to see how charge is deposited on the dielectric surface as the actuator progresses through each of the four distinct phases of operation.

In Figure 13(a) the plasma is quenched at the peak amplitude of the applied waveform (t_1). During this time, the surface potential at all downstream locations is positive. As the applied voltage becomes more negative, the surface potential follows, but only within approximately 1.5 mm from the edge of the exposed electrode.

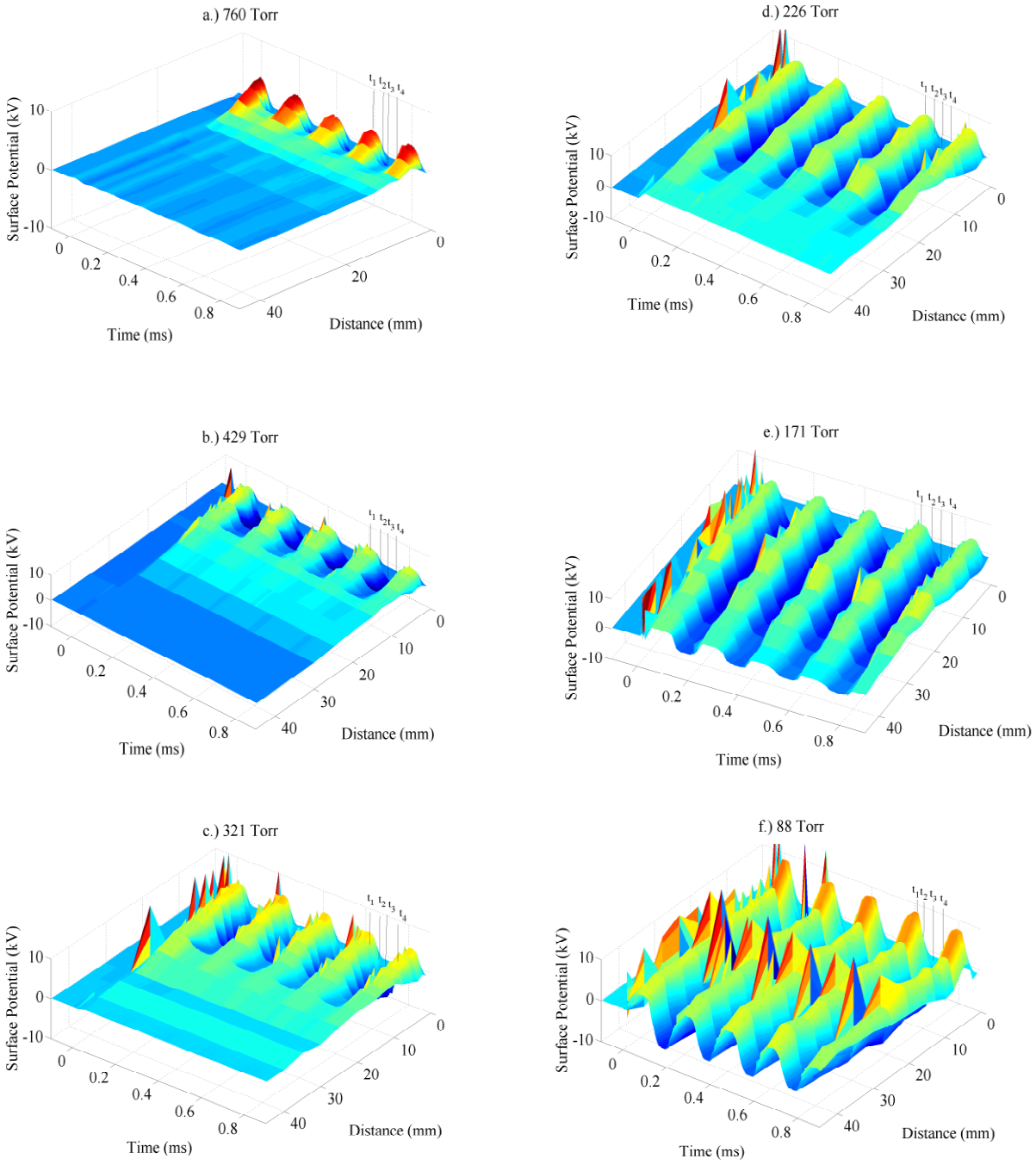

Figure 12. As pressure is decreased and a larger region of plasma is formed, the surface potential on the dielectric surface spreads out from the edge of the exposed electrode.

The potential between 2.00 and 5.00 mm is unchanged until the potential trends to zero far away from the exposed electrode edge. As Enloe *et. al.* states, the change in surface potential close to the exposed electrode is due to the capacitive voltage division and polarization charge on the dielectric surface [24]. The longitudinal electric field derived from the data shown in Figure 13 (a) is shown in Figure 13(b). There is a large portion of the dielectric surface (from approximately x = 5.00 to 14.00 mm) where the electric field is roughly constant at E ≈ 0.2 kV/mm.

From x = 14.00 mm and beyond the electric field trends to zero. As the plasma ignites at time t_2 (Figure 13(c)), the effects of negative charges being carried downstream by the plasma can be seen. As in Figure 13(a), there is a large region of net positive surface potential from approximately x = 3.00 mm and on with a corresponding region of positive electric field (Figure 13(d)) at x = 7.00 mm. During this part of the discharge cycle, the strongest electric field is limited close to the exposed electrode edge (≈ 2.00 mm and closer). At t_3, shown in Figure 13(e) the plasma is again quenched and we can see similarities between the t_1 interval and the t_3 interval. A region of positive surface potential is again established at x = 5.00 mm and remains positive as the surface potential trends to zero far away from the exposed electrode. The electric field (Figure 13(f)) varies most near the exposed electrode (x = 7.00 mm), but remains unperturbed farther downstream as there is no discharge present. As in the previous quenching cycle (between t_1 and t_2) the polarization charge effects are found close to the area nearest the exposed electrode [24]. The plasma reignites in the final phase of the discharge cycle (t_4) and is shown in Figure 13(g) and Figure 13(h). The maximum electric field shown in Figure 13(d) is larger than that shown in Figure 13(h) (1.25 kV/mm and 1.8 kV/mm, respectively) due to the fact that although the applied waveform is symmetric, the surface charge density is not.

In Figure 14 (a-h) the results for 429 Torr are presented. During time t_1 the surface potential shown in Figure 14 (a) follows similar trends to those found in Figure 13 (a). The surface potential follows that of the applied voltage for distances approximately 2 mm and closer to the exposed electrode. The surface potential trends to zero outside the region of constant surface potential between x = 2.00 and 5.00 mm, as is seen in Figure 13 (a). The longitudinal electric field (Figure 14 (b)) does not appear to be constant between x = 2.00 mm and x = 14 mm as is the case in Figure 13 (b). This same region, however, exhibits a local maximum of E ≈ 0.5 kV/mm before trending to zero. When the plasma ignites at t_2 (Figure 14 (c)) the effects of decreased pressure can immediately be seen. When compared with Figure 13 (c), the magnitude of the surface potential at each distinct time step is similar, however the distance downstream that experiences an always net positive surface potential now begins at x = 5.00 mm, whereas before the region of positive surface potential began at x = 3.00 mm. This is evidence that as the plasma sweeps out farther downstream from the exposed electrode at lower pressures the deposited charge is also swept farther downstream. The electric field (Figure 14 (d)) shows a similar shift with a positive electric field being generated from x = 9.00 mm before trending to zero. The magnitude of the electric field is approximately the same when compared with the results from 760 Torr. As the plasma is quenched at t_3 (Figure 14 (e)) the similarities to time t_1 can again be seen. A region of positive surface potential is established from x = 5.00 mm before trending to zero far from the exposed electrode. The electric field (Figure 14 (f)) becomes positive at x = 10 mm, much like during the t_2 interval, before trending to zero. When compared with Figure 13 (f) the magnitude of the electric field remains approximately the same. During the t_4 interval, shown in Figure 14 (g) and Figure 14 (h), the plasma ignites for the second time and again the effect of the decrease in pressure can be seen. The region of positive surface potential is established at x = 5.00 mm, just as in t_2. The electric field remains constant from x = 11.00 mm and further, before trending to zero far away from the exposed electrode. The magnitude of the electric field is smaller during t_4 than in t_2 for the same reasons discussed previously.

The results shown in Figure 15 (a-h) are obtained by operating the actuator at a pressure of 321 Torr. During the t_1 time interval, the plasma is quenched. The surface potential (Figure 15 (a)) remains constant from x = 0.00 mm to x = 5.00 mm. In fact, unlike the pressures previously examined, the surface potential does not just follow the applied potential, but instead either remains constant or shows a slight increase up to x = 4.00 mm. This is most evident in the plots of t_1 + 20 μs and t_1 + 30 μs. This is due to the effects of the capacitive voltage division as well as an increase in polarization charge the actuator experiences close to the exposed electrode. After x = 5.00 mm the surface potential remains largely unchanged before trending to zero as the applied waveform progresses in time. The electric field calculated for this time interval is shown in Figure 15 (b). The electric field remains constant at E ≈ 0.2 kV/mm from x = 5.00 mm until the end of the buried electrode at x = 44.75 mm. When the plasma ignites at t_2, the plasma now (visually) sweeps out to approximately x = 14 mm (as shown in Figure 11). This can be seen in the surface potential shown in Figure 15 (c). Like the pressures shown previously, there is a region in which the dielectric surface acquires an always net positive surface potential which starts at x = 7.5 mm. Interestingly there is a non-zero surface potential over the dielectric surface until x = 44.75 mm (the location of the last V-dot probe on the buried electrode), where at higher pressures the surface potential was approximately zero by x ≈ 15.00 mm. The "dip" in the curve is an artifact of the fitting process used and does not represent anything physical. The electric field during this time interval (Figure 15 (d)) becomes positive at x ≈ 20.00 mm and is relatively constant at E ≈ 0.1 kV/mm. When the plasma again quenches, similar trends emerge that were seen during t_1. The surface potential (Figure 15 (e)) becomes positive at x = 13 mm and remains so over the entire dielectric surface before going to zero at x = 40 mm. The surface potential is largely unchanged after x = 5.00 mm as the applied waveform progress through time, reaching a maximum of 3.5 kV before decreasing gradually to zero. The surface potential follows the

applied potential up to x ≈ 2.00 mm as before, but then begins to decrease slightly until x ≈ 5.00 mm. This is the result of the increased polarization and capacitive voltage division effects discussed previously. The electric field (Figure 15 (f)) during this time interval remains constant over all time intervals after x = 5.00 mm. At positions closer to the exposed electrode ($x < 5.00$ mm) the electric field increases at first (up to x = 2.50 mm) before entering a region of negative electric field between x = 5.00 and 22.5 mm. After x = 22.5 mm the electric field is approximately zero. When the plasma ignites again during t_4 (Figure 15 (g) and Figure 15 (h)) the results of the plasma sweeping out across the dielectric surface can again be seen. For all time intervals the surface potential (Figure 15 (g)) decreases at first where during the time intervals of t_1 and t_1 + 10 μs the surface potential remains negative between x = 2.00 mm and x = 12.5 mm. Between x = 12.5 and 40 mm there is a positive, non-zero, surface potential on the dielectric surface, similar to that of t_2. The electric field (Figure 15 (h)) during this time interval oscillates from zero and 0.05 kV/mm between x = 20.00 and 44.75 mm. Worth noting is that when compared to Figure 14 (h), the electric field shown in Figure 15 (h) becomes negative farther downstream (x = 5.00 mm) and stays negative for a farther downstream distance (out to x = 20.00 mm). At 429 Torr, the electric field during this same time interval becomes negative at x = 2.5 mm and is positive again by x = 10.00 mm. Overall, the electric field strength is weaker at this pressure when compared to the pressures previously discussed.

Plotted in Figure 16 (a-h) are the results with the actuator operating at a pressure of 226 Torr. During t1 (Figure 16 (a)), the surface potential exhibits all of the previously discussed trends and, like the results at 321 Torr, increases up to a distance of x = 10.00 mm where after this point the surface potential begins to decrease. Unlike the pressures examined before, however, the surface potential never goes to zero. In fact, the surface potential is always positive and never falls below a value of 2 kV. The electric field (Figure 16 (b)) is uniform over the entire dielectric surface (except close to the exposed electrode at a position of x = 7.00 mm or less) at a magnitude of E ≈ 0.1 kV/mm before going to zero at x = 40.00 mm. When the plasma ignites at t_2 (Figure 16 (c)) the effect that the large region of plasma formation has on the surface potential distribution on the dielectric surface is highly evident. The spread of surface potential between t_2 and t_2 + 30 μs is much larger than the previously discussed pressures. The potential increases up to a value of 6.0 kV at x = 7.00 mm during t_2. Between x = 7.00 and 17.00 mm the surface potential remains constant before falling off (during t_2). After x = 15.00 mm the surface potential is always positive and non-zero. The corresponding electric field (Figure 16 (d)) after x = 10.00 mm is approximately constant, varying slightly between 0 kV/mm and 0.10 kV/mm. During time t_3, when the plasma quenches for the second time, similar trends discussed before are seen in the surface potential (Figure 16 (e). The surface potential remains largely unchanged throughout this time period downstream of x = 5.00 mm. Note that the dielectric surface does not acquire a region of positive surface potential until after x = 27.5 mm. At the previously discussed pressure of 321 Torr during this same time interval (Figure 15 (e)) the region of positive surface potential was established at a distance of x = 15.00 mm. The electric field (Figure 16 (f)) at this time shows similar trends to those discussed for Figure 16 (a). Here, however, the electric field is constant from x = 7.00 mm to 30.00 mm with E ≈ -0.3 kV/mm. The electric field never returns to a positive value before going to zero at x = 44.75 mm. This is the first time that the electric field is largely negative over the entirety of the dielectric surface. When the plasma ignites for the second time during t_4, a region of constant positive surface potential is established at x ≈ 27.50 mm. The surface potential never goes to zero far away from the exposed electrode edge, maintaining a value of 2 kV at x = 44.75 mm. The electric field (Figure 16 (h)) is mostly negative between x = 10.00 mm and 35 mm. During the time interval of t_4 + 30 μs the electric field goes positive at x = 22.5 mm up to a value of 0.4 kV/mm before trending back to zero.

When the plasma is quenched during t_1 at a pressure of 171 Torr (Figure 17 (a)) the surface potential remains constant at 6 kV out to a distance of x = 20 mm before beginning to decrease. The corresponding electric field (Figure 17 (b)) is approximately zero from x = 5.00 mm until the end of the buried electrode. A local maximum of E = 0.2 kV/mm at a downstream distance of x = 25 mm is seen, but this is an artifact of the fitting routine used on the data. Once the plasma ignites the effect the plasma has on sweeping the charge across the dielectric surface is readily seen. A region of always positive surface potential is established at x = 30 mm. The electric field (Figure 17 (d)) remains mostly constant throughout this time interval, oscillating between 0.5 kV/mm and -0.5 kV/mm. At t_3 there is never a region on the dielectric surface where the surface potential (Figure 17 (e)) is always positive. The electric field exhibits a local maximum at x = 2.5 mm downstream, but then trends to zero. The electric field between x = 6.00 mm and 17.00 mm is approximately zero before going negative between x = 17.00 mm and 45.00 mm. Between all of the time intervals the surface potential, as well as the electric field, does not vary much. In (Figure 17 (g)) the effect the plasma has on the distribution of the surface potential is seen again. During each time step between x = 10.00 mm and 30.00 mm, the surface potential remains constant. The electric field (Figure 17 (h)) decreases from 1.5 kV/mm to zero by x = 5.00 mm and remains approximately zero over the entirety of the dielectric surface.

At a pressure of 88 Torr, the same trends when the actuator is operating at a pressure of 171 Torr are seen during each of the time intervals. During t_1 (Figure 18 (a,b)) there is a region between x = 5.00 mm and 25.00 mm that has a constant surface potential of 6 kV. The corresponding electric field during this time interval is zero after x = 5.00 mm. Similar trends to that shown at 171 Torr are seen again as the plasma ignites at t_2 (Figure 18 (c,d)).When the plasma quenches again at t_3 (Figure 18 (e,d)) the surface potential is constant at -6.0 kV over nearly all of the dielectric surface, only beginning to increase at a downstream location of x = 35.00 mm. Just like in the case of 171 Torr, there is no region of positive surface potential that is established on the dielectric surface. Again, the electric field has a non-zero value only close to the exposed electrode edge before going to zero at x = 10.00 mm. Once the plasma forms for the second time (Figure 18 (g,h)) the plasma sweeps the charge across the dielectric, remaining constant for each time interval between x = 5.00 mm and x = 45 mm. At t_4 + 10 μs the surface potential remains positive across the dielectric surface, with an approximately constant value of 1.75 kV. The electric field exhibits similar behavior as that shown in the time interval of t_2. The polarization effects are seen close to the exposed electrode edge, but the majority of the dielectric surface experiences an electric field of 0 kV/mm. The electric field does take on a small negative magnitude at x = 35.00 mm, however this trend cannot be captured due to the lack of V-dot probes after x = 44.75 mm.

C. Average Surface Potential and Charge Transferred

To better understand how the surface potential is distributed across the dielectric surface the average surface potential at each V-dot probe location was calculated. This is done by taking the average over a set number of applied AC signals (in this experiment, 4 periods) after equilibrium has been established. The results of this analysis are shown in Figure 19 with error bars shown where appropriate. Similar conditions to those found in [24] are used in this work as the same material (Macor) was used as the dielectric material, as well as similar high voltage signals (13.4 $kV_{pk\text{-}pk}$ 5 kHz sine wave in [24]). Figure 19 (a) shows that at 760 Torr the surface potential reaches a maximum value of 2.5 kV at a downstream location of x = 6.00 mm. Enloe *et. al.* found that for similar conditions the largest surface potential to be 1.67 kV at approximately 7.5 mm downstream [24]. At pressures of 429, 321, and 226 Torr the maximum average surface potential reaches a value of 3.0 kV at positions of x = 15, 20, and 40 mm, respectively. This shows that as the pressure decreases the region of largest surface potential moves farther downstream from the exposed electrode. During this same span of pressure drops, the width of the average surface potential also grows. At 760 Torr, there is a region of net positive potential from the exposed electrode edge (x = 0 mm) to x = 20.00 mm downstream. This region extends to x = 35 mm at 429 Torr until reaching the end of the V-dot probe array at x = 44.75 mm by 321 Torr. The entire dielectric surface maintains the net positive average surface potential at pressures of 171 Torr and 88 Torr.

Looking at Figure 19 (e) and (f), there is no peak surface potential downstream, indicating that the location of the peak surface potential has moved so far downstream that our V-dot probes are no longer able to capture it. Interestingly though, these plots do exhibit the smaller peak close to the exposed electrodes edge that begins to appear at 321 Torr. This local maximum is always located at approximately x = 2.5 mm downstream, regardless of the ambient pressure conditions. The amplitude of the maximum, however, is varied having a range of values of 0.75 kV, 0.45 kV, 0.6 kV, and 1.75 kV corresponding to the pressures from 321 Torr down to 88 Torr, respectively. The capacitive voltage division/polarization of the dielectric plays a much greater role in the buildup of surface potential near the edge of the exposed electrode. The fact that there is a local maximum close to the electrode edge and that it grows in magnitude, but does not move downstream (like the peak of the maximum average surface potential does) indicates that the polarization of the dielectric becomes stronger as the pressure is decreased. A discussion of this can be found later in this paper.

The results shown in Figure 20 (a-f) depict how the average physical charge is deposited downstream as the ambient pressure is changed. Much like the average surface potential, the maximum charge transferred moves downstream as pressure decreases. In fact, the location for the peak charge transferred corresponds directly to the location of the peak average surface potential at a given pressure**.** This is to be expected as the contributions from the capacitive voltage division/polarization effects diminish far from the electrodes edge, meaning the only meaningful mechanism for building up surface potential is through physical charge deposition.

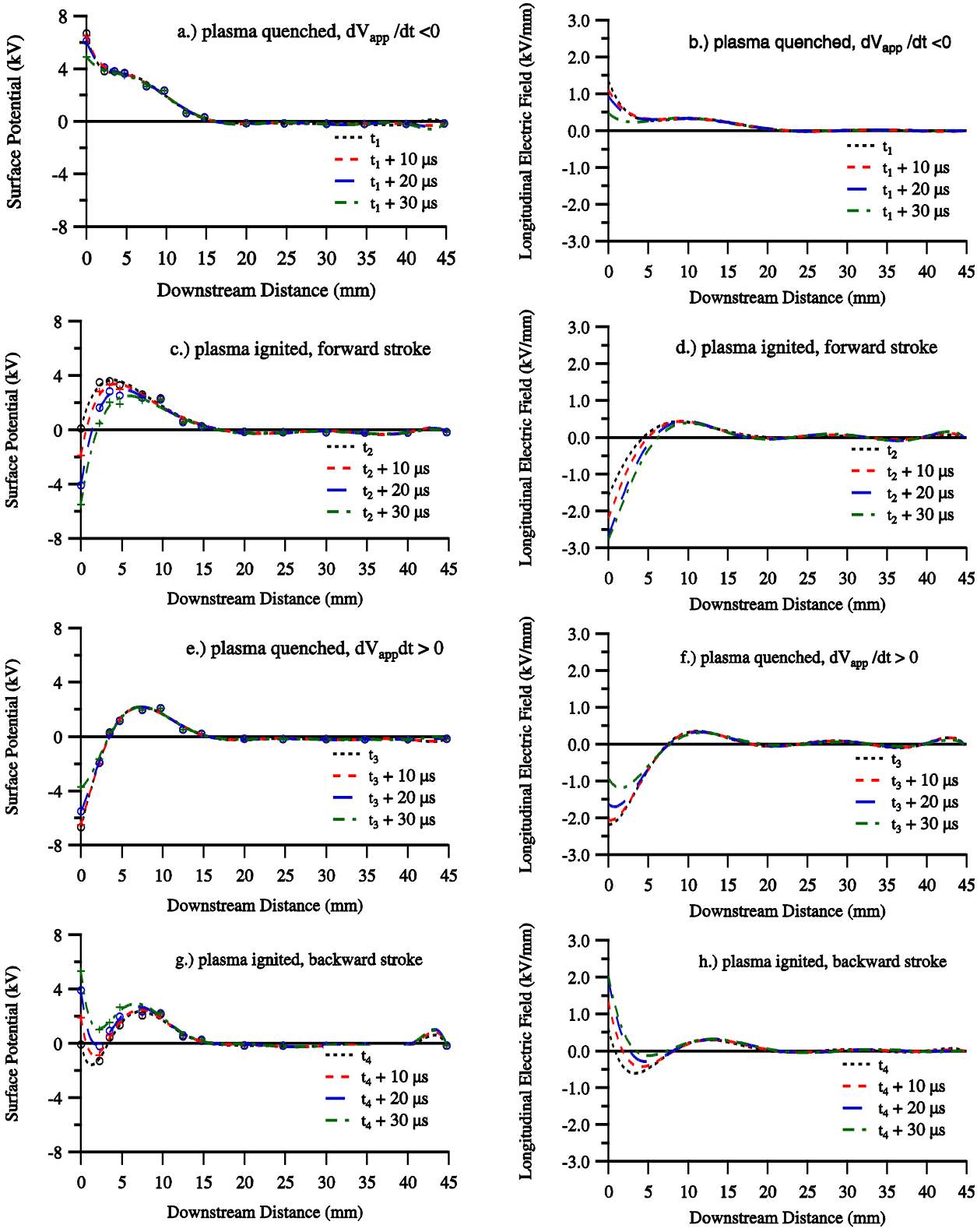

Figure 13. Plots a-h show the temporal evolution of the surface potential and electric field at discrete downstream points for an operating pressure of 760 Torr.

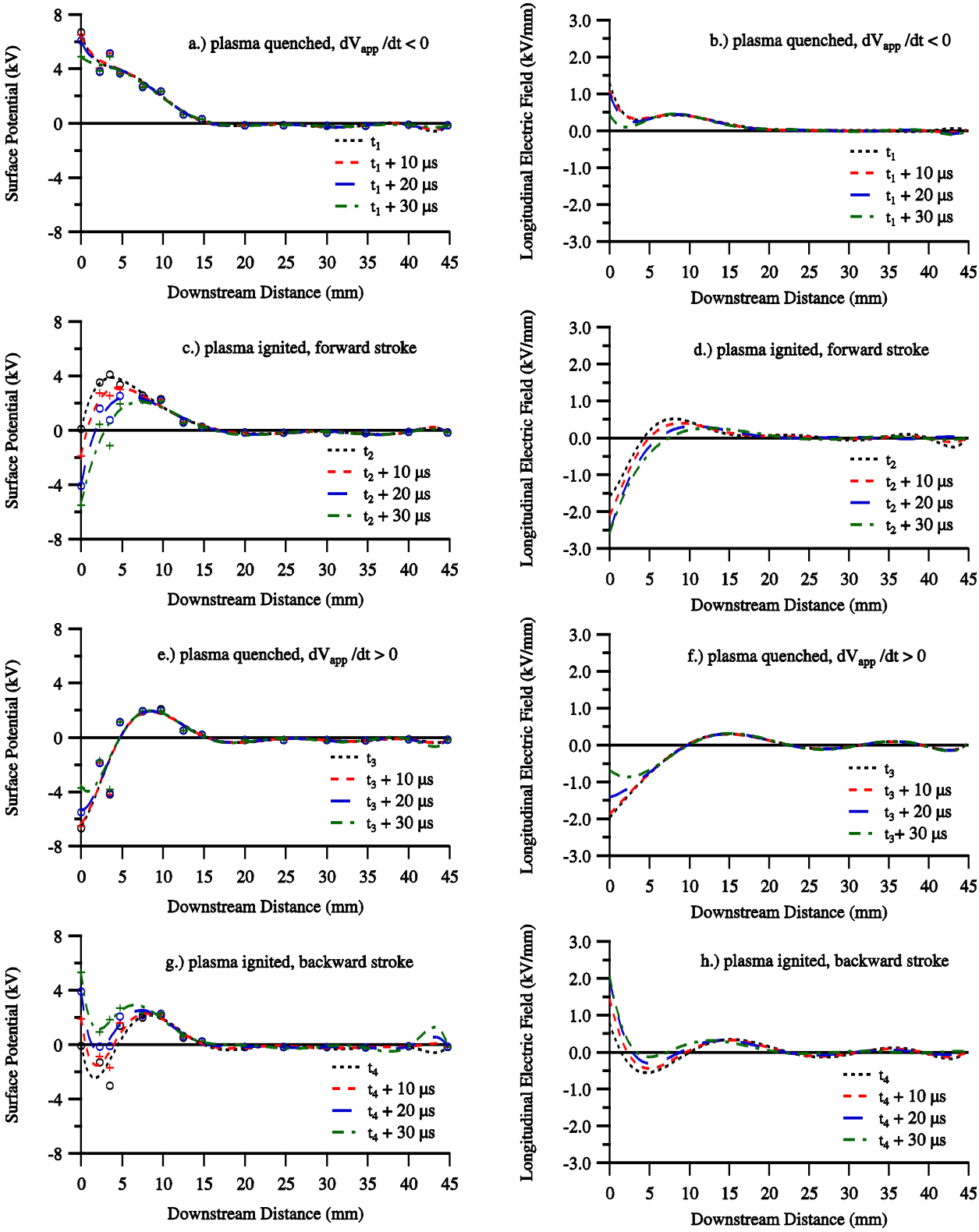

Figure 14. Plots a-h show the temporal evolution of the surface potential and electric field at discrete downstream points for an operating pressure of 429 Torr.

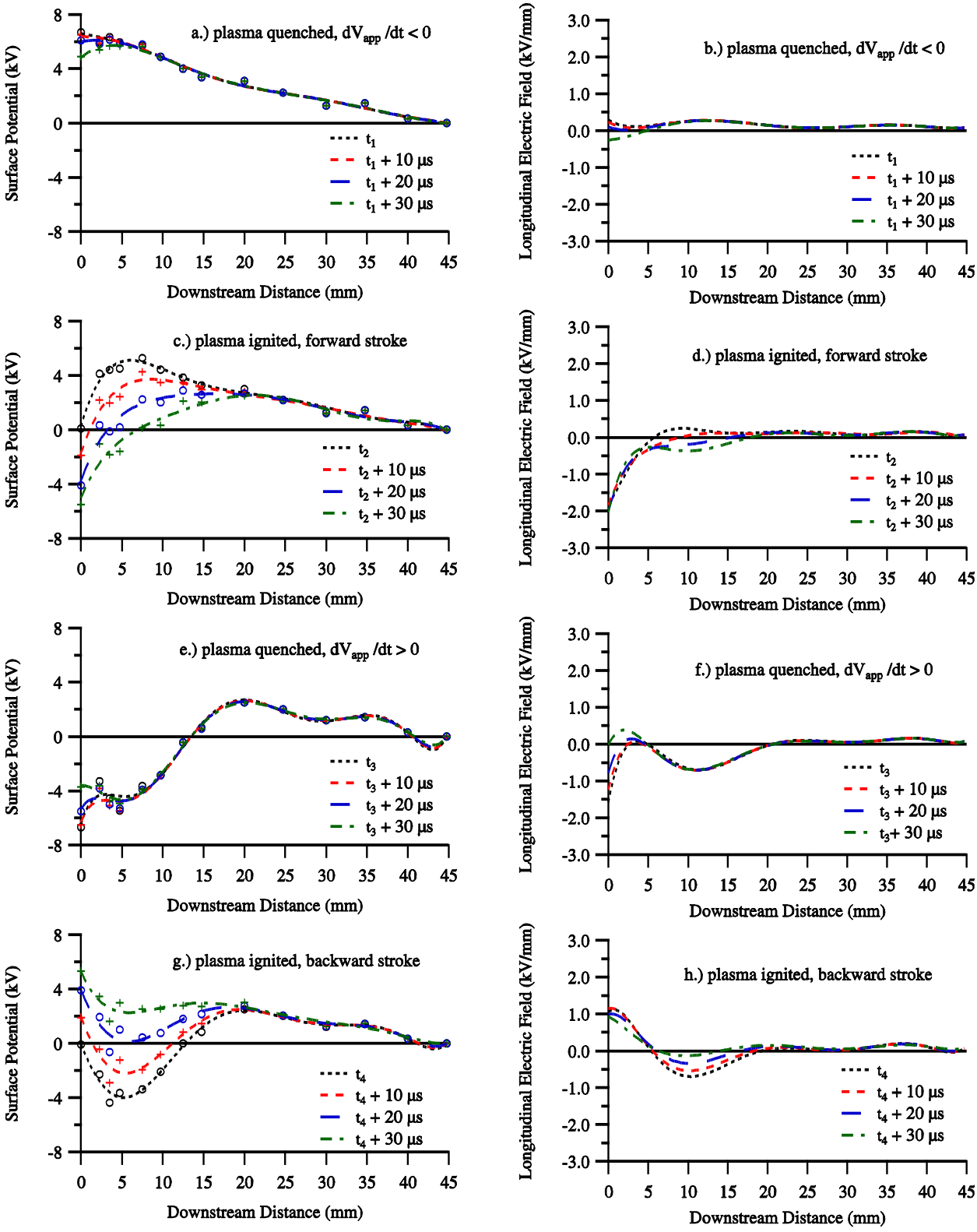

Figure 15. Plots a-h show the temporal evolution of the surface potential and electric field at discrete downstream points for an operating pressure of 321 Torr.

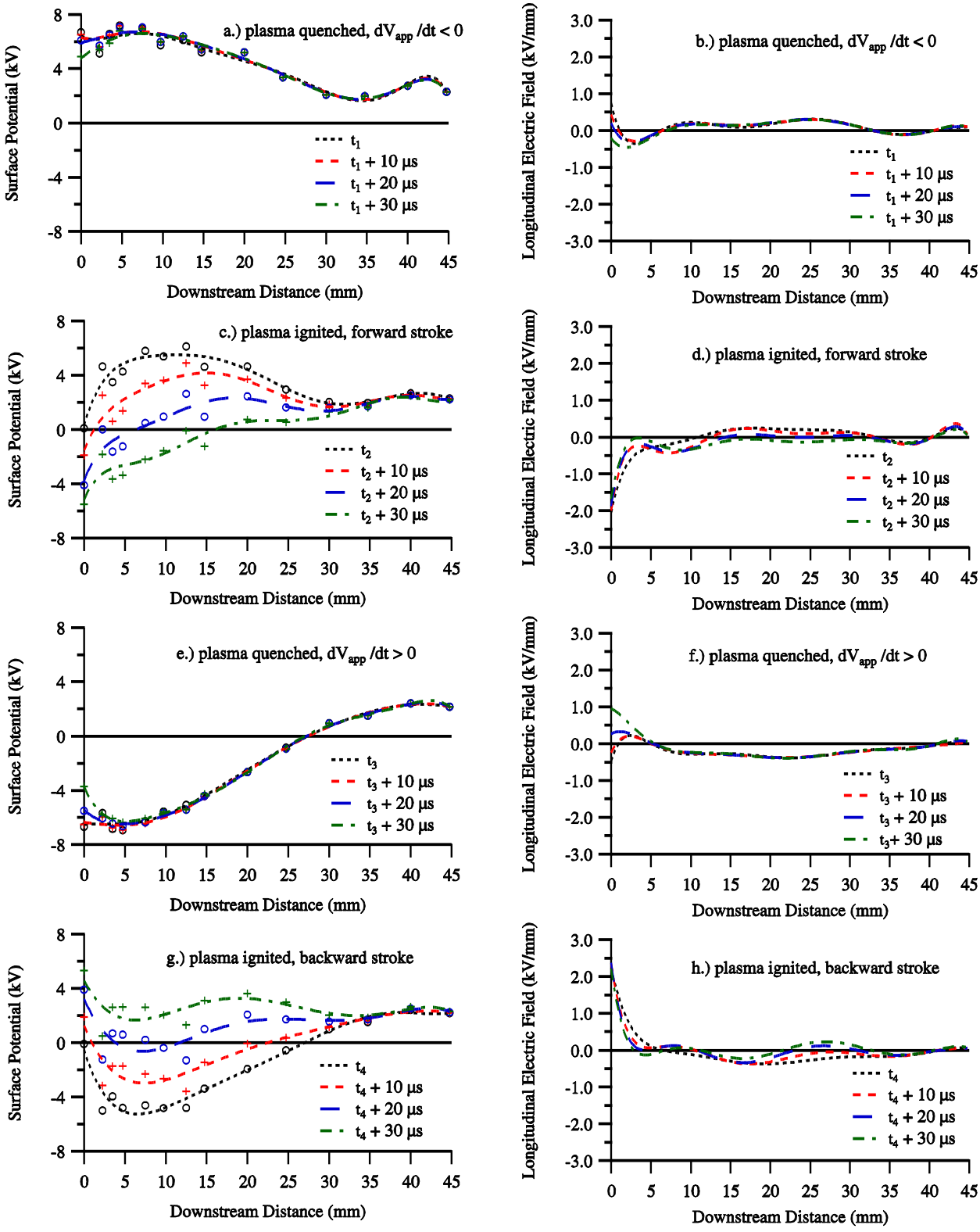

Figure 16. Plots a-h show the temporal evolution of the surface potential and electric field at discrete downstream points for an operating pressure of 226 Torr.

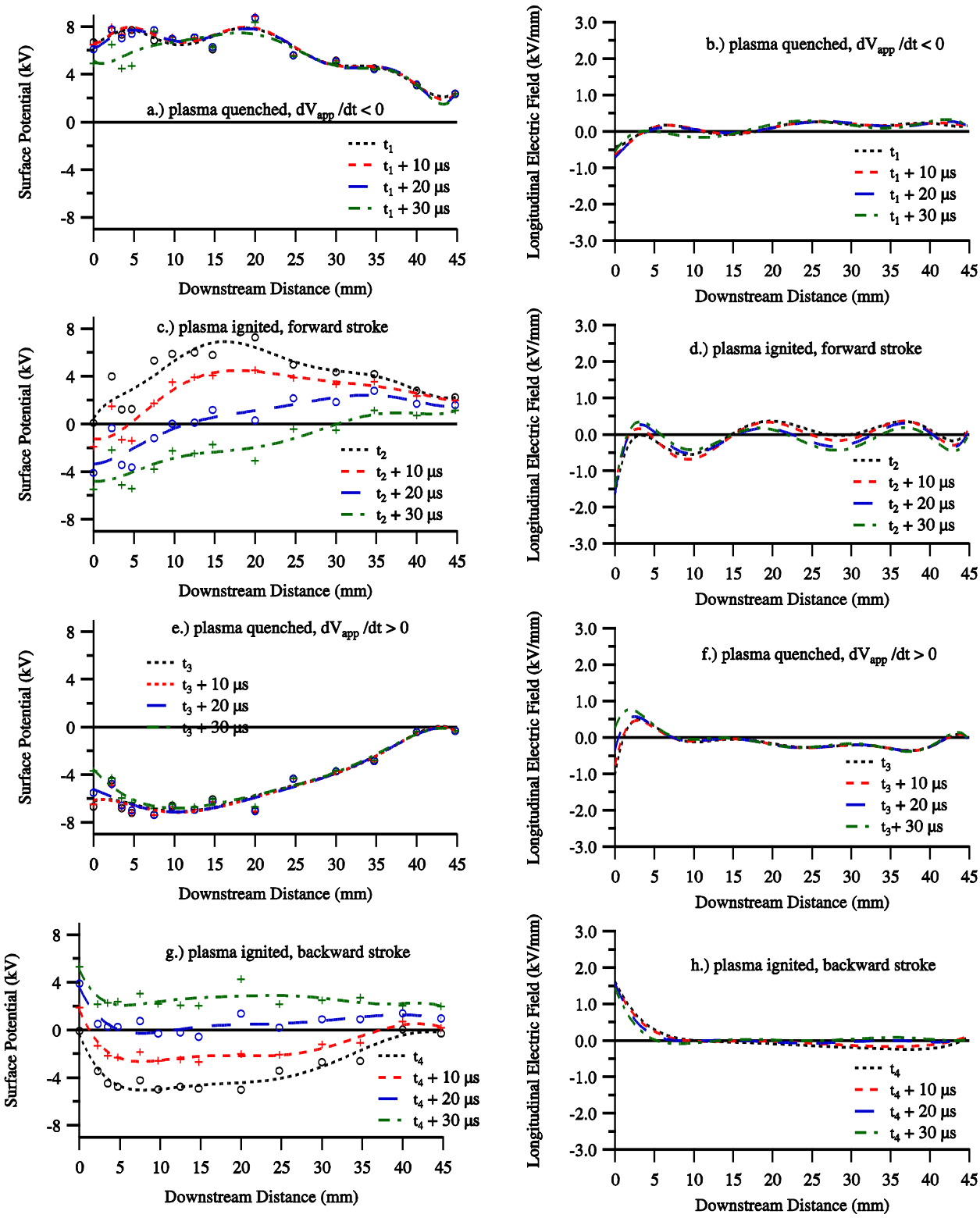

Figure 17. Plots a-h show the temporal evolution of the surface potential and electric field at discrete downstream points for an operating pressure of 171 Torr.

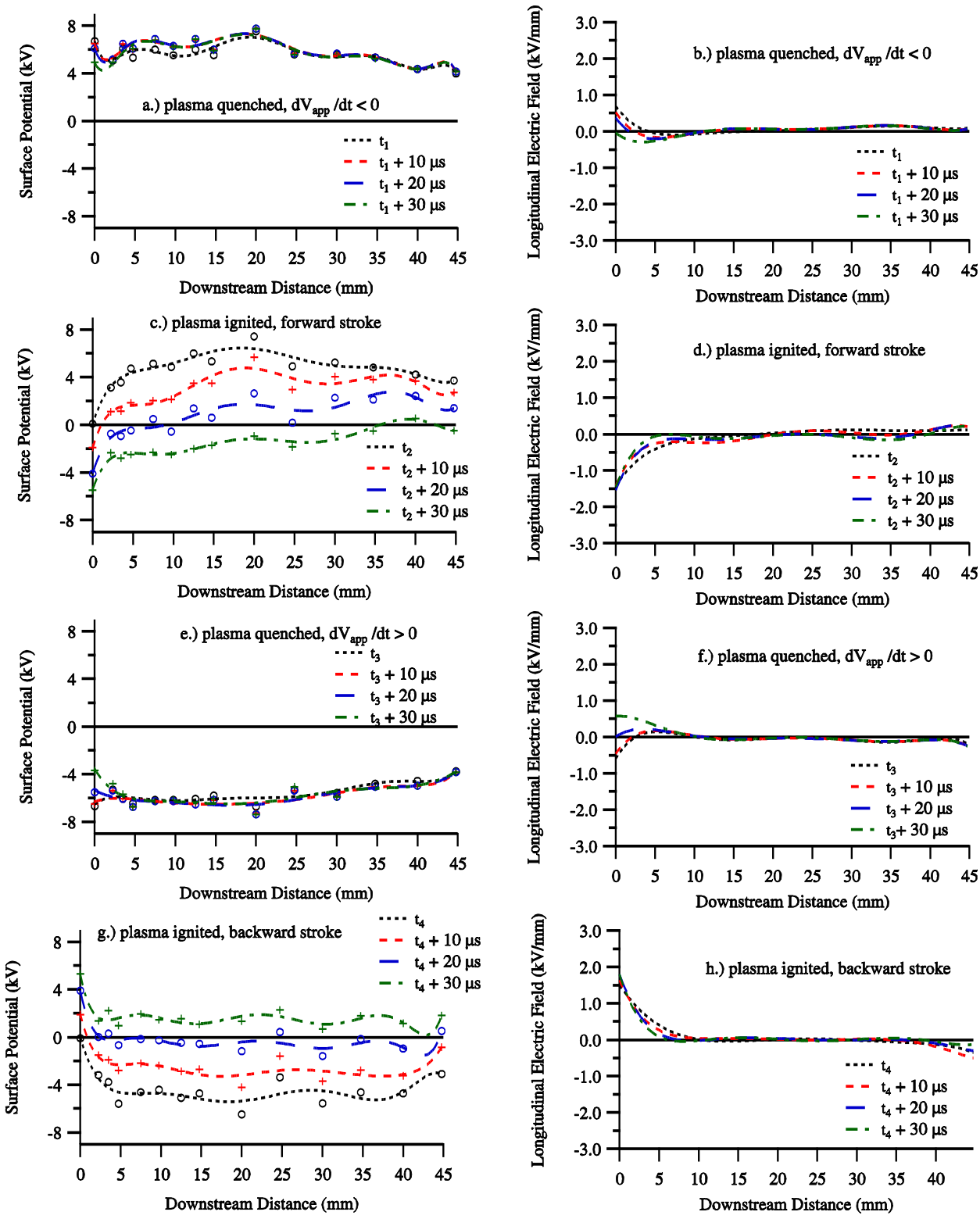

Figure 18. Plots a-h show the temporal evolution of the surface potential and electric field at discrete downstream points for an operating pressure of 88 Torr.

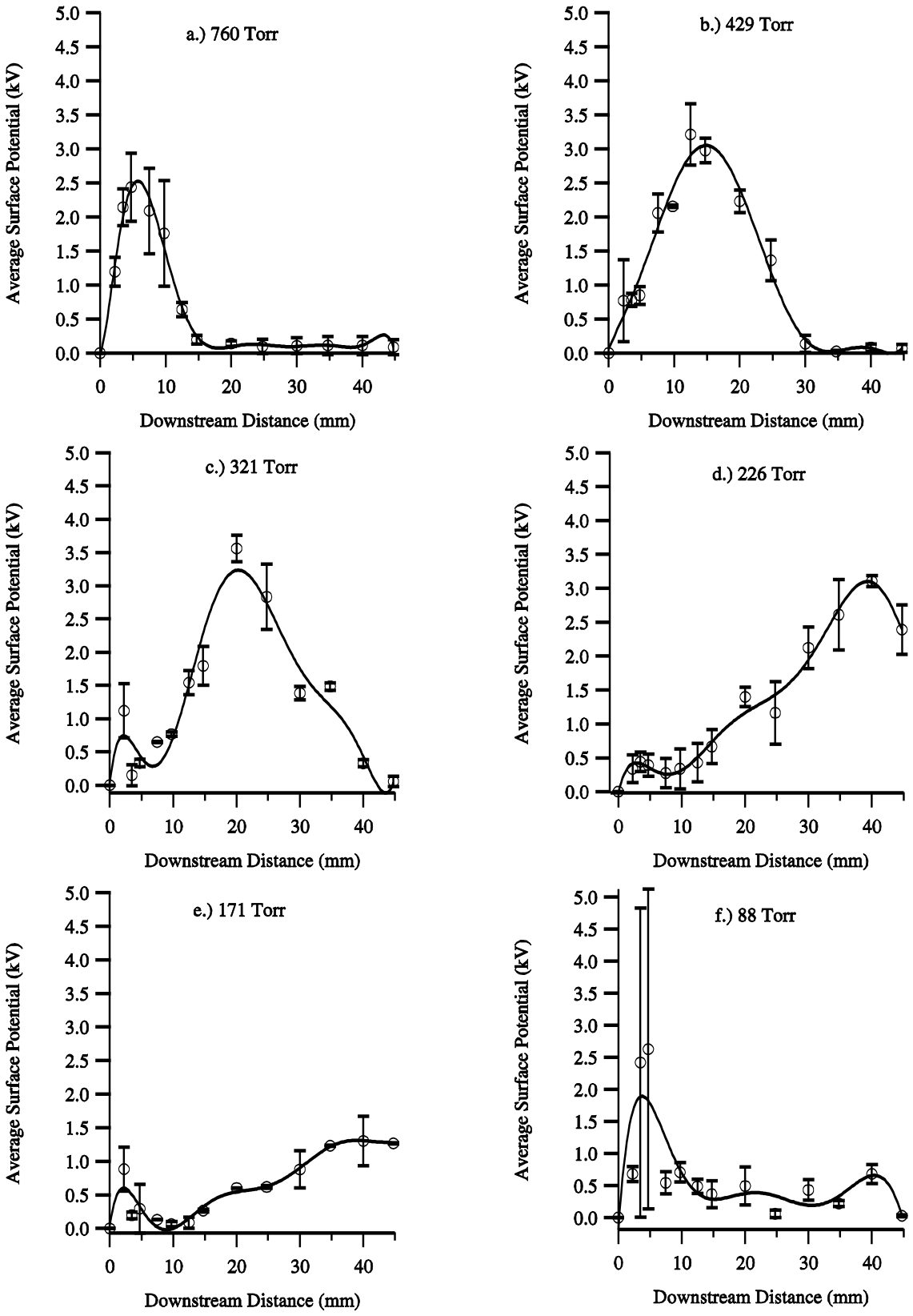

Figure 19. The average surface potential on the dielectric surface moves further from the exposed electrode edge as the pressure is decreased.

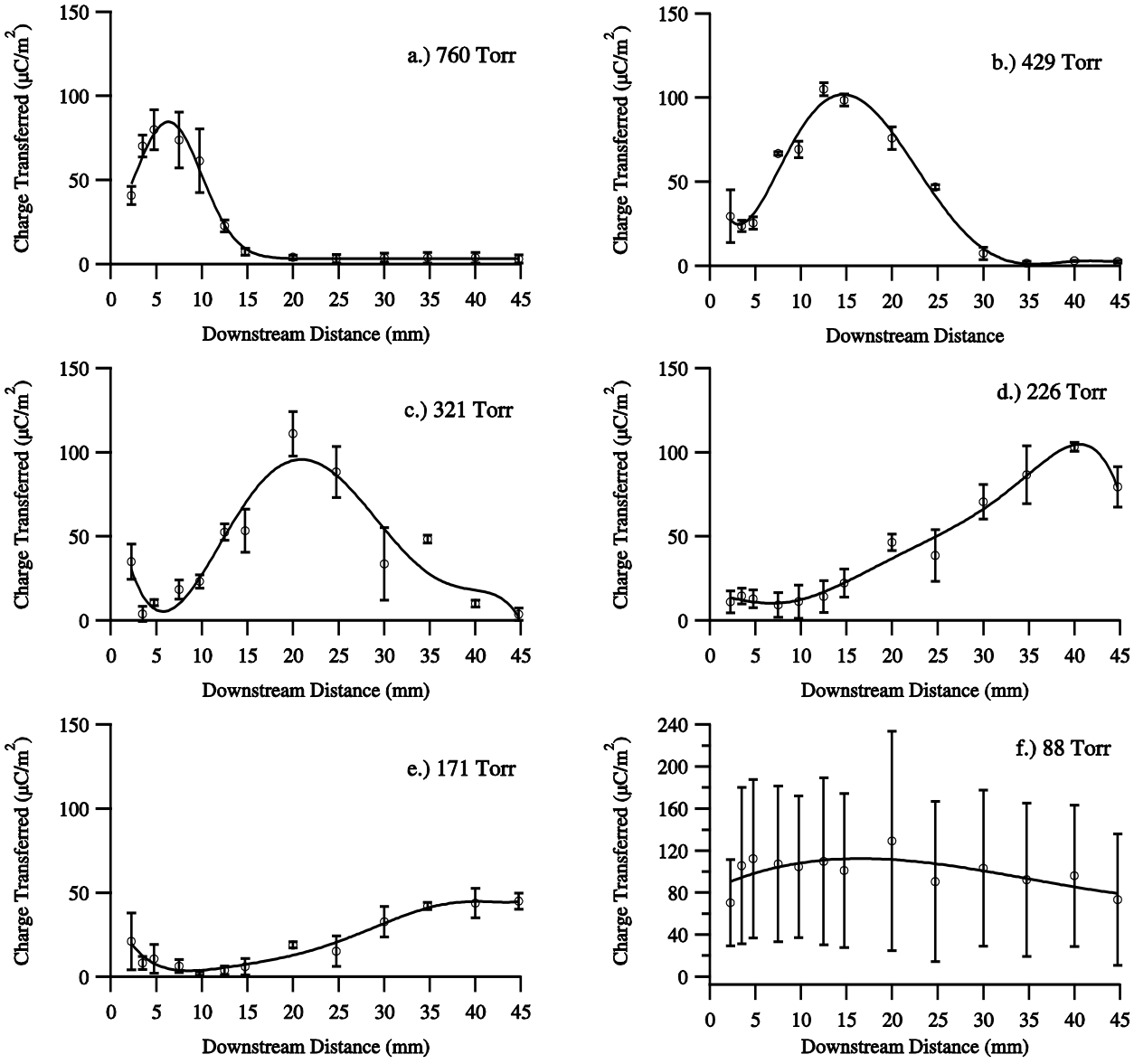

Figure 20. Plots a-f show the average physical charge deposition transferred per AC cycle as a function of the downstream distance for different pressures.

IV. Discussion

The overall trends and effects that ambient pressure has on the surface potential of the dielectric and electric field generated are presented here. Figure 21 shows the location of the peak average surface potential and peak charge transferred as a function of pressure. Only those pressures down to 226 Torr are plotted due to the fact that at lower pressures the maximum average surface potential has moved past our farthest V-dot probe. The polarization effect that contributes to the overall surface potential is mainly seen at downstream distances of 2.5 mm or less, where the electric field is the strongest. This means that the dominant mechanism for building surface potential at downstream distances that are far from the leading edge of the exposed electrode is physical charge deposition. This is confirmed by Figure 21. Further, the maximum average surface potential and charge transferred are inversely proportional to the pressure.

The trends that the experimentally determined electric field exhibit are in good agreement with the work done by Gregory *et al.* [14]. Though the electric field close to the exposed electrode (downstream distance of 5.00 mm or less) changes little as pressure decreases, the electric field far from the electrode is largely zero after a pressure of 171 Torr. In fact, at 88 Torr approximately 78% of the dielectric surface (above the buried electrode) has an electric field of zero. This is significant when compared with the results from 760 Torr, as at that pressure only 55% of the dielectric surface has an electric field of zero. When you take into account the fact that at 88 Torr there is 800% more plasma in the downstream direction than there is at 760 Torr, it becomes evident that the majority of power the actuator is drawing is going into making plasma, and not accelerating it. This implies that the induced force created by the plasma at far downstream locations will go to zero at lower pressures. These results further strengthen the assumption that the location for the majority of the force production is located near the exposed electrode.

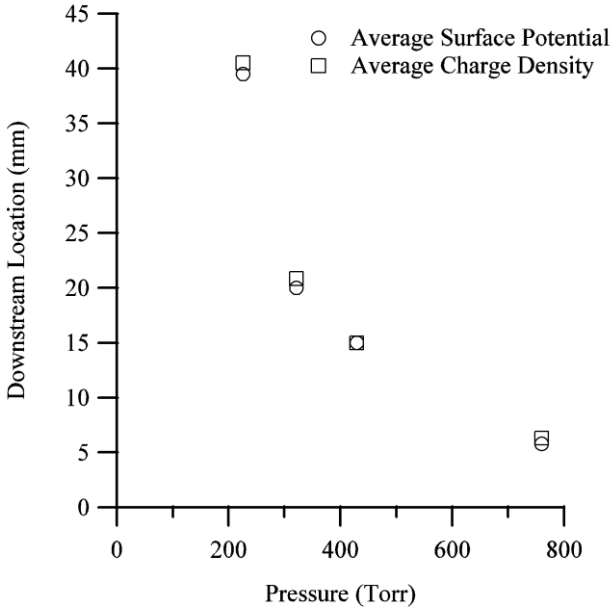

Figure 21. The location of the maximum average surface potential and charge transferred moves downstream as pressure decreases in a similar non-linear fashion seen in Figure 10.

V. Conclusion

In this paper we have presented measurements done with an array of capacitive V-dot probes of the potential on the dielectric surface. We show that while the surface potential is spread out across the dielectric surface as pressure decreases, the electric field remains largely unchanged close to the exposed electrode edge. At distances far from the exposed electrode the electric field is zero for a larger percentage of the dielectric surface when compared to those results obtained at 760 Torr. This suggests that at far downstream distances the power being used by the actuator is spent generating plasma and not accelerating it. This explains why force production and, subsequently, the efficiency of the actuator decreases with decreasing pressure.

References

1. C.L. Enloe, G.I.F., T.E. McLaughlin, Robert D. VanDyken, K.D. Kachner, Eric J. Jumper, and Thomas C. Corke, *Mechanisms and Responses of a Single Dielectric Barrier Plasma Actuator: Plasma Morphology.* AIAA Journal, 2004. **42**(3): p. 6.
2. Moreau, E., *Airflow control by non-thermal plasma actuators.* Journal of Physics D: Applied Physics, 2007(40): p. 33.
3. Jerome Pons, E.M.a.G.T., *Asymmetric surface dielectric barrier discharge in air at atmospheric pressure: electrical properties and induced airflow characteristics.* Journal Of Physics D: Applied Physics, 2005. **38**: p. 9.
4. Thomas C. Corke, C.L.E., and Stephen P. Wilkinson, *Dielectric Barrier Discharge Plasma Actuators for Flow Control.* Annual Review of Fluid Mechanics, 2009. **42**: p. 27.
5. Corke, M.L.P.T.C., *Separation control on high angle of attack airfoil using plasma actuators.* AIAA Journal, 2004. **42**: p. 8.
6. Corke, C.H.T.C., *Plasma Flaps and Slats: An Application of Weakly Ionized Plasma Actuators.* Journal of Aircraft, 2009. **46**(3): p. 10.
7. Post, T.C.C.M.L., *Overview of Plasma Flow Control: Concepts, Optimization, and Applications.* 43rd AIAA Aerospace Sciences Meething and Exhibit, 2005: p. 15.
8. Mertz, T.C.C.B., *Plasma Flow Control Optimized Airfoil.* 44th AIAA Aerospace Sciences Meething and Exhibit, 2006: p. 13.
9. Mehul P. Patel, T.T.N., Srikanth Vasudevan, *Plasma Actuators for Hingeless Aerodynamic Control of an Unmanned Air Vehicle.* 3rd AIAA Flow Control Conference, 2008: p. 21.

10. Flint O. Thomas, T.C.C., Muhammad Iqbal, Alexey Kozlov, David Schatzman, *Optimization of Dielectric Barrier Discharge Plasma Actuators for Active Aerodynamic Flow Control.* AIAA Journal, 2009. **47**(9): p. 10.
11. M. Forte, J.J., J. Pons, E. Moreau, G. Touchard, M. Cazalens, *Optimization of a dieletric barrier discharge actuator by stationary and non-stationary measurements of the induced flow velocity: application to airflow control.* Exp. Fluids, 2007. **43**: p. 12.
12. J. Reece Roth, X.D., *Optimization of the Aerodynamic Plasma Actuator as an Electrohydrodynamic (EHD) Electrical Device.* 44th AIAA Aerospace Sciences Meething and Exhibit, 2008: p. 28.
13. Ryan Durscher, S.R., *Novel Multi-Barrier Plasma Actuators for Increased Thrust.* 48th AIAA Aerospace Scieneces Meeting and Exhibit Including the New Horizons Forum and Aerospace Exposition, 2010: p. 9.
14. James W. Gregory, C.L.E., Gabriel I. Font, and Thomas E. McLaughlin, *Force Production Mechanisms of a Dielectric-Barrier Discharge Plasma Actuator*, in *45th AIAA Aerospace Sciences Meeting and Exhibit*, `, Editor. 2007, AIAA 2007-185: Reno, Nevada. p. 13.
15. V.M. Litvinov, V.V.S., and A.A. Uspenskii, *Role of the Static Pressure in Experiments on Flow Control by Means of Surface Capacitor Discharges.* Fluid Dynamics, 2006. **41**(2): p. 6.
16. N. Benard, N.B., and E. Moreau, *Electric Wind Produced by a Single Dielectric Barrier Discharge Actuator Operating in Atmospheric Flight Conditions - Pressure Outcome.* 39th Plasmadynamics and Lasers Conference, 2008: p. 16.
17. N. Benard, N.B.a.E.M., *Electric wind produced by a surface dielectric barrier dishcarge operating in air at different pressures: aeronautical control insights.* Journal of Physics D: Applied Physics
2008. **41**: p. 5.
18. Yun Wu, Y.L., Min Jia, Huimin Song, Zhigang Guo, Ximing Zhu, and Yikang Pu, *Influence of operating pressure on surface dielectric barrier discharge plasma aerodynamic actuation characteristics.* Applied Physics Letters, 2008. **93**`: p. 3.
19. Takashi Abe, Y.T., Shunichi Sato, and Nobara Kimura, *Experimental Study for Momentum Transfer in a Dielectric Barrier Discharge Plasma Acutator.* AIAA Journal, 2008. **46**(9): p. 9.
20. N. Benard, E.M., *Effects of Altitude on the Electromechanical Characteristics of a Single Dielectric Barrier Discharge Plasma Actuator.* 41st Plasmadynamics and Lasers Conference, 2010: p. 17.
21. Philippe Versailles, V.G.-G., and Huu Duc Vo, *Impact of Pressure and Temperature on the Performance of Plasma Actuators.* AIAA, 2010. **48**(4): p. 5.
22. C.L. Enloe, M.G.M., and T.E. McLaughlin, *Time-correlated force production measurements of the dielectric discharge plasma aerodynamic actuator.* Journal of Applied Physics, 2008. **103**(073302): p. 7.
23. C.L. Enloe, T.E.M., J.W. Gregory, R.A. Medina, and W.S. Miller, *Surface Potential and Electric Field Structure in the Aerodynamic Plasma Acutator*, in *46th AIAA Aerospace Sciences Meeting and Exhibit*. 2008, AIAA 2008-1103: Reno, Nevada. p. 11.
24. C.L. Enloe, G.I.F., T.E. McLaughlin, and D.M. Orlov *Surface Potential and Longitudinal Electric Field Measurements in the Aerodynamic Plasma Actuator.* AIAA Journal, 2008. **46**(11): p. 11.
25. G.I. Font, C.L.E., T.E. McLaughlin, and D. Orlov, *Plasma Discharge Characteristics and Experimentally Determined Boundary Conditions for a Plasma Actuator*, in *45th AIAA Aerospace Sciences Meeting*. 2007, AIAA 2007-0188: Reno, Nevada. p. 14.
26. Dmitry F. Opaits, G.N., Sohail H. Zaidi, Mikhail N. Schneider, Richard B. Miles, Alexandre V. Likhanskii, Sergey O. Macheret, *DBD Plasma Actuators Driven by a Combination of Low Frequency Bias Voltage and Nanosecond Pulses.* 48th AIAA Aerospace Scieneces Meeting and Exhibit, 2008(AIAA 2008-1372): p. 18.